Searching for $(\gamma, \alpha)/(\gamma, n)$ branching points in the γ-process path near $A = 100$

R. Kelmar ◉, A. Simon,* O. Olivas-Gomez ◉, P. Millican ◉, C. S. Reingold, E. Churchman ◉, A. M. Clark ◉,
S. L. Henderson ◉, S. E. Kelly, D. Robertson ◉, E. Stech, and W. P. Tan

Department of Physics and The Joint Institute for Nuclear Astrophysics, University of Notre Dame, Indiana 46556-5670, USA

Four (α, γ) cross-section measurements on stable nuclei in the $A = 100$ mass range were performed at the University of Notre Dame Nuclear Science Laboratory. The ^{102}Pd$(\alpha, \gamma)^{106}$Cd and ^{110}Cd$(\alpha, \gamma)^{114}$Sn reactions were measured for the first time. The ^{90}Zr$(\alpha, \gamma)^{94}$Mo and ^{108}Cd$(\alpha, \gamma)^{112}$Sn results extended the measured range down to energies lower than those of the previous experiments. These reactions were studied as possible branching points in γ-process reaction networks. The measured cross-section values were compared to the NONSMOKER database as well as to calculations performed with TALYS 1.9. The combination of parameters available in TALYS that gave the best fit to the data was found and the corresponding reaction rates were obtained. The inverse (γ, α) rates were then obtained and compared to the corresponding (γ, n) rates to investigate the relative strength between the two reaction pathways. It was found that in all four cases the (γ, α) reaction pathway begins to dominate within the 1.5–3.5 GK temperature range.

I. INTRODUCTION

The nucleosynthesis mechanisms for heavy nuclei are an important area of research in nuclear astrophysics. In Ref. [1], three processes were proposed for the formation of the heavy nuclei, the r-, s-, and p-processes. The r- and s-processes are responsible for the formation of the majority of the heavy isotopes above Fe. The p-process is a mechanism for the formation of the 35 proton-rich p-nuclei that cannot be formed by the r- and s-processes. These nuclei are "shielded" from the r- and s-processes by the valley of stability.

In Ref. [1], the p-process was proposed as a series of proton captures on stable nuclei during type Ia and type II supernova shock waves. However, more recent work [2] has shown that the density and temperature conditions within supernovas are unlikely to be sufficient to reproduce the observed p-nuclei abundances. Alternatively, another proposed scenario of the p-process is that of photodisintegration through the γ-process. This process spans a mass region from roughly $A = 80$ to 200.

To model different γ-process reaction networks many input parameters are needed. Information about the astrophysical location as well as nuclear properties must be incorporated. One important piece of information is the nuclear reaction rates for all of the isotopes involved in the reaction network. The most relevant reactions for the γ-process are (γ, n), (γ, p), and (γ, α). Due to experimental limitations, many of these reaction rates cannot be measured in the laboratory. Therefore the development of models that can accurately predict the reaction rates is important for furthering understanding the γ-process.

These reaction networks comprise thousands of different reactions, meaning that it is not feasible to measure all of the reactions. To identify reactions that have the largest impact on the reaction flows, sensitivity studies are performed. One recent sensitivity study by Rauscher [3] investigated the branching points in reaction flows. These branching points are the location along an isotopic chain where either the (γ, p) reaction or the (γ, α) reaction begins to dominate over the (γ, n) reaction. These locations are critical in determining which isotopes are made in the γ-process. The branching points are also highly sensitive to temperature, and so it is important to determine the temperatures at which the branchings begin to occur.

The study by Rauscher identified several key (α, γ) reactions to measure. Included in those suggestions were the ^{102}Pd$(\alpha, \gamma)^{106}$Cd and ^{108}Cd$(\alpha, \gamma)^{112}$Sn reactions as a first priority and the ^{90}Zr$(\alpha, \gamma)^{94}$Mo reaction as a second priority. In this work all three of these were measured. Additionally ^{110}Cd$(\alpha, \gamma)^{114}$Sn was measured.

The experimental details are presented in Sec. II. The cross-section values obtained in this work are given and compared to literature values in Sec. III. The TALYS calculations performed are discussed in Sec. IV. The best-fit model is determined and the corresponding reaction rates are calculated. The impact these results have on the branching temperatures of the isotopes is discussed in Sec. V. Finally, the conclusions are discussed in Sec. VI.

II. EXPERIMENTAL METHOD

The experiment was conducted at the University of Notre Dame Nuclear Science Laboratory (NSL) [4] using the 10-MV FN Tandem Accelerator. A beam of ^{4}He^{2+} particles with energies between 7.5 and 12 MeV was impinged

TABLE I. The thickness and enrichment of the four targets as well as the Q value of the (α, γ) reactions.

Isotope	Thickness (μg/cm^2)	Enrichment (%)	(α, γ) Q value (MeV)
^{90}Zr	969(48)	98(1)	2.066 45(18)
^{102}Pd	1589(79)	78.15(5)	1.653 88(123)
^{108}Cd	2100(100)	69.33(5)	1.827 56(115)
^{110}Cd	2130(110)	97.36(2)	2.636 67(38)

upon targets of isotopically enriched ^{90}Zr, ^{102}Pd, ^{108}Cd, and ^{110}Cd. The beam current ranged from 5 to 50 nA and was monitored throughout the experiment by using the beam pipe surrounding the target as a Faraday cup. The beam current was chosen to maximize the count rate during the experiment while minimizing the detector dead time. The detector dead time was kept below 1% throughout the experiment.

The thicknesses of the ^{102}Pd, ^{108}Cd, and ^{110}Cd self-supported foil targets were measured at the NSL using Rutherford backscattering spectrometry (RBS). All were analyzed using the SIMNRA software package [5]. The ^{90}Zr target was loaned from the National Superconducting Cyclotron Laboratory. Details on this target can be found in Ref. [6]. The target properties are detailed in Table I. The enrichment of the material was provided by the vendor, the National Isotope Development Center [7].

The ^{102}Pd target was mounted on the target holder with a tungsten backing. Both ^{108}Cd and ^{110}Cd were mounted on the target holder with a tantalum backing. These backings were used to reduce background from beam straggling and from interaction of scattered beam with the beam pipe and the target holder material.

The targets were placed in the center of the High EfficienCy TOtal absorption spectrometeR (HECTOR). HECTOR is composed of 16 NaI(Tl) segments each read by two photomultiplier tubes. For more details on HECTOR, see Ref. [8]. These 16 detectors cover nearly the 4π solid angle allowing for the use of the γ-summing technique [9]. The large angular coverage leads to a high efficiency to absorb all of the γ rays emitted in a cascade. The spectrum then consists of a single peak known as the "sum peak." The energy of the sum peak is given by

$$E_\Sigma = E_{\text{c.m.}} + Q, \tag{1}$$

where $E_{\text{c.m.}}$ is the center-of-mass energy of the system and Q is the Q value of the reaction.

An example of an experimental sum peak for each reaction is given in Fig. 1. Also shown in Fig. 1 are the fits to the sum peaks as well as the final subtracted histograms. All four sum peaks are for a beam energy around 12 MeV. At these energies the background is composed of cosmic rays, neutrons interacting with the detector crystals, and interactions with the target backings. To account for the background the peaks are fit with a Gaussian and a second-order polynomial function. The second-order polynomial fit to the background can then be subtracted off to obtain the integral of the sum peak. In the top panel of Fig. 2 the sum peak and the second-order polynomial that is used to fit the background are shown. Once the background has been subtracted the sum peak is integrated to obtain the number of events, N_Σ. This method is different than the method described in Ref. [8]. The beam-induced background in the sum-peak area observed from the (α, γ) reactions was much higher than what is typically observed in the case of proton-capture reactions. Additionally, the shape of the background on the high-energy side of the sum peak resulted in an incorrect background estimation. For that
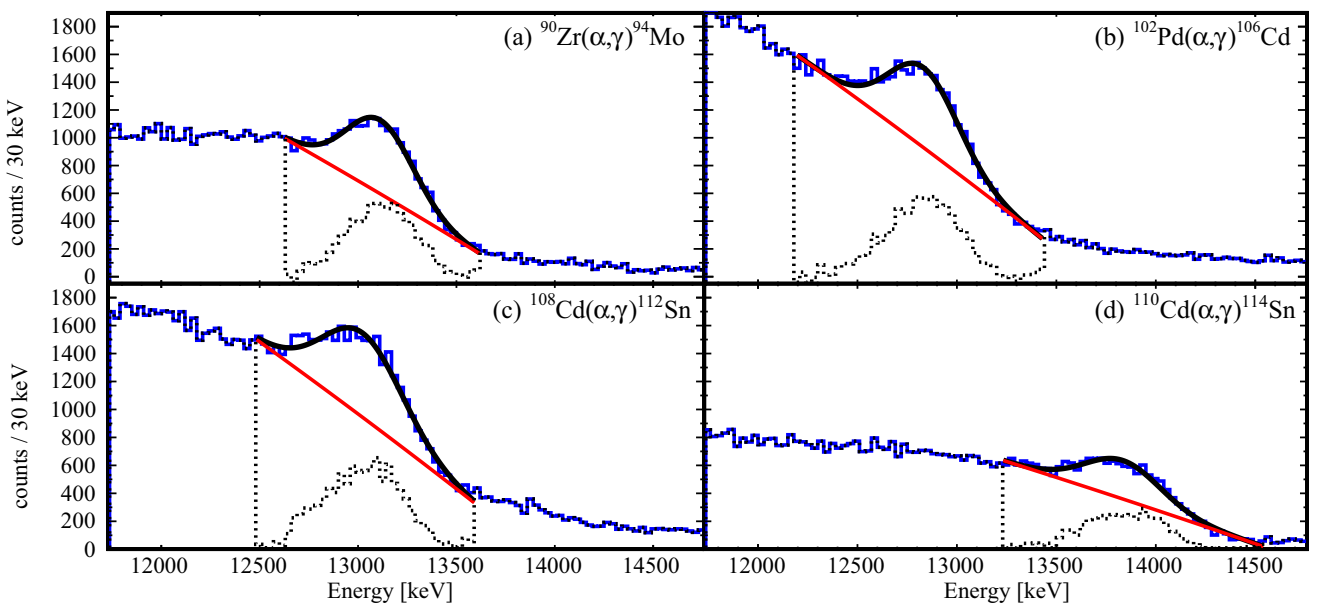

FIG. 1. Example sum spectra for the four reactions with a beam energy around 12 MeV. The fit to the data is shown as well as the background fit (red, straight line) and the subtracted histogram (black, dashed line).
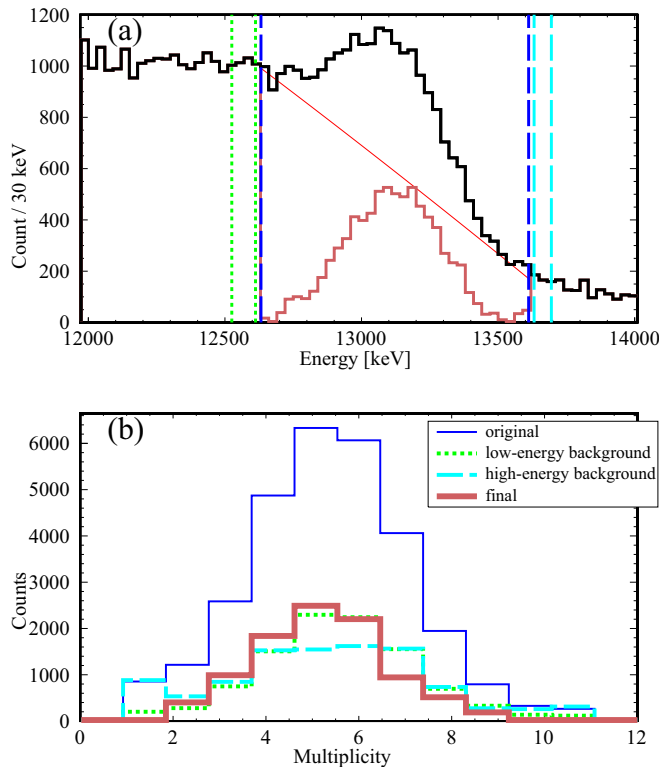
FIG. 2. An example of how the multiplicity histogram was obtained for the sum spectrum produced from the ^{90}Zr$(\alpha, \gamma)^{94}$Mo reaction with an energy of $E_{\mathrm{c.m.}} = 11.31$ MeV. In panel (a), the area of the sum peak that is integrated is indicated by the dark blue lines. The regions that are selected as representative of the background are indicated by the green and light blue lines. In panel (b), the colored histograms correspond to the region indicated in panel (a). The red (thicker) histogram shows the multiplicity histogram that is left after the subtraction. This histogram is used to determine the average multiplicity of the sum peak.

reason, a second-order polynomial was introduced to describe the background under the sum peak consistently throughout all the measured data points. This small correction was used to increase the robustness of the fit and reduce the uncertainty in the background estimations. As can be seen in Fig. 1, the fits still visually appear to be linear.

The total cross section can then be calculated using

$$\sigma = \frac{N_\Sigma}{N_b n_t \varepsilon_\Sigma}, \qquad (2)$$

where N_b is the total number of beam particles, n_t is the areal target density, and ε_Σ is the summing efficiency. The summing efficiency is calculated as a function of both the sum-peak energy and the average multiplicity $\langle M \rangle$ of the events in the sum peak. The multiplicity is the number of segments that fired in a given event. The summing efficiency functions were determined using GEANT4 simulations which are detailed in Ref. [8]. Because the background below the sum peak generally consisted of many more counts than the sum peak, the multiplicity of the background had to be subtracted from the multiplicity of the summed region. This was done by subtracting the average multiplicity of events just below and

TABLE II. Measured cross-section values for the four (α, γ) reactions. The $E_{\mathrm{c.m.}}$ reported is the energy at the center of the target.

$E_{\mathrm{c.m.}}$ (MeV)	σ (μb)	$E_{\mathrm{c.m.}}$ (MeV)	σ (μb)
		^{90}Zr	
11.31(05)	253(47)	8.64(05)	27.4(7.5)
10.99(05)	175(46)	8.26(05)	18.9(5.9)
10.48(05)	151(34)	7.65(05)	15.9(7.6)
9.99(05)	115(20)	7.60(05)	14.3(6.4)
9.46(05)	60(14)	7.56(05)	13.4(6.1)
9.08(05)	49(14)	7.52(05)	7.5(4.2)
		^{102}Pd	
11.47(05)	151(28)	10.01(05)	30.5(6.9)
10.99(05)	89(20)	9.52(05)	19.6(5.9)
10.49(05)	41(11)	8.88(05)	13.6(5.4)
		^{108}Cd	
11.54(06)	122(22)	8.97(06)	7.8(2.2)
11.02(06)	62(13)	8.88(06)	7.7(2.9)
10.50(06)	35.5(7.5)	8.79(06)	6.8(2.5)
10.02(06)	16.7(3.4)	8.71(06)	7.3(2.4)
9.50(06)	14.2(3.2)	8.61(06)	4.7(1.8)
9.17(06)	12.4(5.5)	8.53(06)	3.9(1.6)
9.07(06)	11.8(2.6)	8.43(06)	5.5(2.0)
		^{110}Cd	
11.55(05)	38.2(8.6)	10.53(02)	10.1(3.1)
11.02(02)	22.5(9.5)	10.06(02)	2.7(2.3)

just above the sum peak in energy, an example of which can be seen in Fig. 2.

Each of the components of the cross-section formula has an uncertainty which is accounted for in the uncertainty of the cross section. Both the number of beam particles and the target density have a systematic uncertainty of 5%. The uncertainty in the number of events in the sum peak consists of both the statistical uncertainty from the number of events and the uncertainty in the fit. This was generally between 8% and 45% for measurements at low energies. The relative uncertainty of the summing efficiency ranged from 10% to 15%.

Also part of the cross-section uncertainty is derived from the change in the cross section over the range of the energy uncertainty. The change was calculated from the best-fit models to each reaction, which are described in Sec. IV. This uncertainty was then incorporated into the error propagation formula for the cross-section uncertainty. This uncertainty generally accounted for less than 2% of the total uncertainty except for the data points at lower energies where there was a steep change in the cross section. In those cases this uncertainty added at most 26% to the uncertainty.

The uncertainty in the center-of-mass energy comes from a combination of the uncertainty in the beam energy resolution, the beam energy definition, and the energy loss through the target. The beam resolution from the tandem pelletron has an uncertainty of 1–2 keV, the beam energy definition's uncertainty was estimated to be up to 20 keV and the energy loss through the targets ranged between 20 and 60 keV.
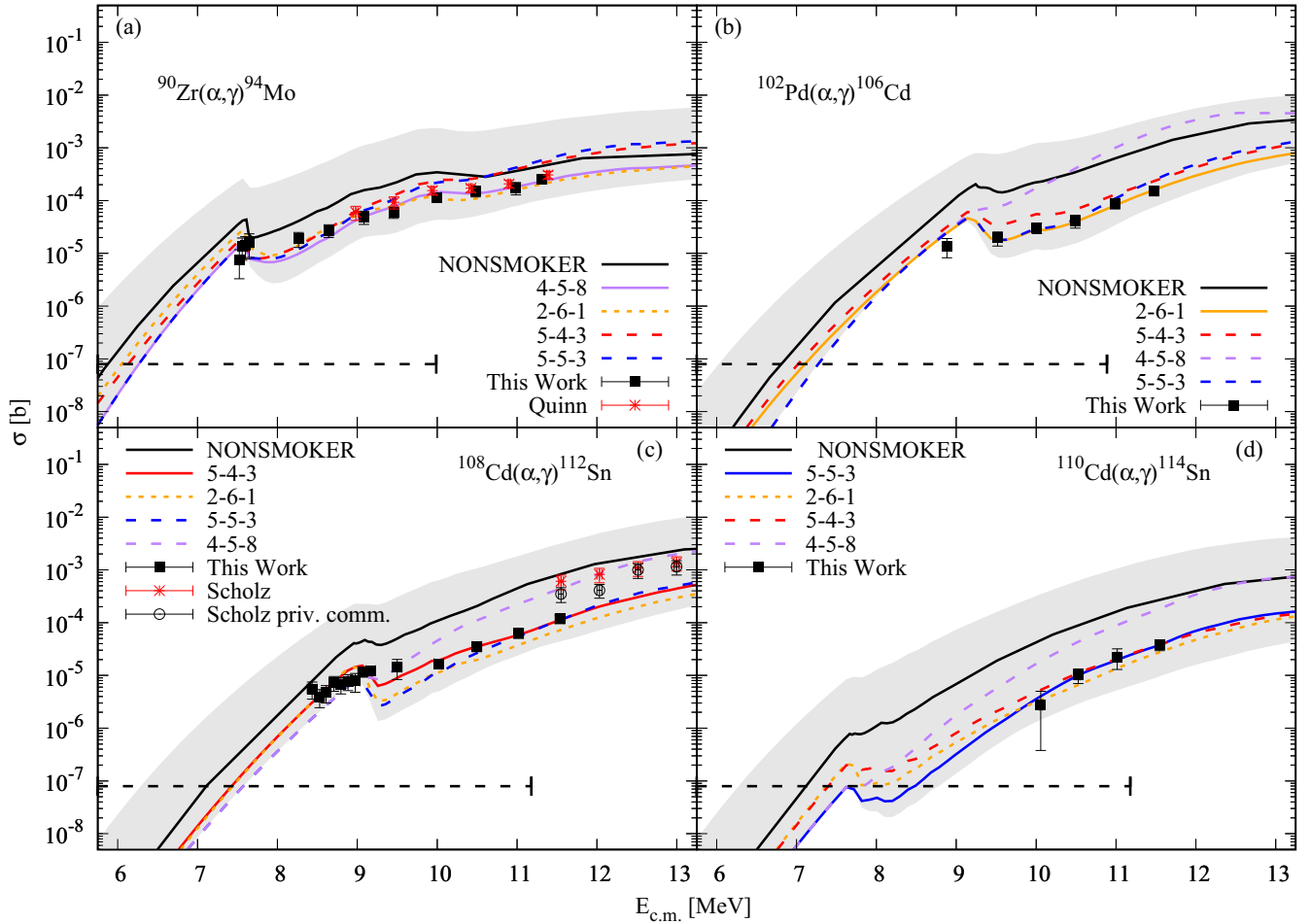
FIG. 3. Cross-section measurements for (a) ^{90}Zr$(\alpha, \gamma)^{94}$Mo, (b) ^{102}Pd$(\alpha, \gamma)^{106}$Cd, (c) ^{108}Cd$(\alpha, \gamma)^{112}$Sn, and (d) ^{110}Cd$(\alpha, \gamma)^{114}$Sn obtained in this work (solid squares), literature values (asterisks) [6,10], and unpublished work (open circles) [11]. In the combinations of three numbers the first number corresponds to a level-density model, the second number is an α-optical-model potential, and the third number is a γ-strength-function model available in TALYS. The models that these refer to are described in the text. The gray shaded area indicates the range of cross sections predicted by different combinations of TALYS parameters. The solid black line shows the prediction from the NONSMOKER code. The solid colored line shows the TALYS calculations for the parameter combination that gives the best fit to the data for the individual reaction. The yellow line shows the TALYS calculations for the parameter combination 2-6-1, which gives the best fit for all of the reactions. The long dashed lines show the TALYS calculations for the parameter combinations that give the best fit for the other reactions measured. The black dashed line indicates the Gamow window for the reaction.

III. RESULTS

Cross-section values obtained for the four reactions at $E_{\text{c.m.}}$ are listed in Table II. The cross sections are plotted in Fig. 3 along with the previous measurements for the ^{90}Zr$(\alpha, \gamma)^{94}$Mo [6] reaction and the ^{108}Cd$(\alpha, \gamma)^{112}$Sn [10] reaction. Good agreement is seen in the case of the ^{90}Zr$(\alpha, \gamma)^{94}$Mo cross-section values. The measurements reported here extend the range beyond the work of Quinn *et al.* [6] down to 7.5 MeV.

The previously measured ^{108}Cd$(\alpha, \gamma)^{112}$Sn cross sections are higher than the results discussed here by a factor of 5 at the overlap point in the data sets. The work of Ref. [10] is based on measurements of only two transitions, from the first 2^+ state to the ground state and from the second 2^+ state to the ground state. The discrepancy in the cross section may be a result of an incomplete level scheme of ^{112}Sn and incorrect γ-branchings that the analysis in Ref. [10] depends on. Another

possible discrepancy might stem from contributions to the line resulting from the transitions from the second 2^+ state to the ground state. As can be seen in Fig. 2 of Ref. [10], the peak is not as convincing as the first 2^+ state to the ground state transition and the measurements have not excluded additional contribution to this line from other reaction channels. The cross sections that are obtained from just the first 2^+ state to the ground state are also plotted in Fig. 3. In this case the discrepancy is less than a factor of 3 [11]. A possible contribution may also stem from the determination of the target thickness as discussed in the paper.

IV. TALYS CALCULATIONS

In all cases, the measured cross sections fall below the predictions from the NONSMOKER code [12]. This is not

TABLE III. Upper portion gives χ^2 thresholds for each of the measured reactions. For details on how these thresholds were calculated, see the text. The bottom portion gives the calculated χ^2 values for different model combinations. In the combination names the first number corresponds to the level density model used, the second number is the α-optical model potential used, and the third number is the γ-strength function used.

	^{90}Zr	^{102}Pd	^{108}Cd	^{110}Cd
10%	3.43	0.99	2.11	0.36
20%	13.38	3.95	8.43	1.45
30%	30.10	8.89	18.97	3.26
50%	83.61	24.70	52.70	9.07
2-6-1	47.19	0.52	38.85	3.69
4-5-8	16.75	7981.62	580.44	478.92
5-4-3	203.50	38.10	15.16	1.44
5-5-3	209.23	11.99	31.69	0.43

surprising as the α-optical-model potential (αOMP) used in the NONSMOKER calculations has been shown to overpredict cross-section values [13]. These measured cross sections can then be compared to different Hauser-Feshbach calculations using the TALYS 1.9 package [14]. Several input combinations were run for each reaction to find the combination of level density (LD), αOMP, and γ-ray-strength function (γSF) that best reproduced all of the data. The TALYS 1.9 package has six different LD models, eight different αOMP models, and eight different γSF models.

There are three macroscopic LD models:

(1) the constant temperature with Fermi gas model [15],

(2) the back-shifted Fermi gas model [16], and
(3) the generalized super fluid model [17,18].

There are also three microscopic LD models included:

(1) microscopic level densities calculated using a Skyrme force from Goriely's tables [19],
(2) microscopic level densities calculated using a Skyrme force from Hilaire's combinatorial tables [20], and
(3) microscopic level densities calculated using a Gogny force from Hilaire's combinatorial tables [21].

The default LD model is the constant temperature with Fermi gas model.

The αOMP models available are as follows:

(1) the proton and neutron optical potentials of Koning and Delaroche [22] modified for α particles,
(2) the α-optical potential of McFadden and Satchler [23],
(3) the double-folding potential of Demetriou, Grama, and Goriely [13] where experimental data were used to constrain the imaginary part of the potential consisting of only a volume component,
(4) the same as (iii) but with a surface and volume component to the imaginary potential,
(5) the same as (iii) and (iv) but a dispersion relation was used to relate the real and imaginary potentials,
(6) the αOMP from Avrigeanu *et al.* [24],
(7) the αOMP of Nolte *et al.* [25], and
(8) the αOMP of Avrigeanu *et al.* [26].

The default is the αOMP of Avrigeanu *et al.* [24], which is option (vi).

TABLE IV. Recommended (α, γ) reaction rates for the four reactions measured. All reaction rates were calculated using the TALYS 1.9 code with the back-shifted Fermi gas LD model, the αOMP from Avrigeanu *et al.* [24], and the Brink-Axel Lorentzian γSF. The uncertainties are based upon the χ^2 percentage that the model achieves for each reaction.

|	$N_A \langle \sigma v \rangle$ (cm^3 mol^{-1} s^{-1})			
T (GK)	^{90}Zr	^{102}Pd	^{108}Cd	^{110}Cd
0.3	$1.90(72) \times 10^{-47}$	$3.97(32) \times 10^{-53}$	$1.94(83) \times 10^{-55}$	$3.3(1.1) \times 10^{-55}$
0.4	$2.32(88) \times 10^{-40}$	$2.62(21) \times 10^{-45}$	$6.3(2.7) \times 10^{-47}$	$6.8(2.2) \times 10^{-47}$
0.5	$2.29(87) \times 10^{-35}$	$7.11(57) \times 10^{-40}$	$2.7(1.2) \times 10^{-41}$	$2.91(93) \times 10^{-41}$
0.6	$1.42(54) \times 10^{-31}$	$9.91(80) \times 10^{-36}$	$5.0(2.1) \times 10^{-37}$	$5.3(1.7) \times 10^{-37}$
0.7	$1.48(56) \times 10^{-28}$	$2.02(16) \times 10^{-32}$	$1.25(54) \times 10^{-33}$	$1.28(41) \times 10^{-33}$
0.8	$4.5(1.7) \times 10^{-26}$	$1.07(09) \times 10^{-29}$	$7.8(3.4) \times 10^{-31}$	$7.8(2.5) \times 10^{-31}$
0.9	$5.4(2.1) \times 10^{-24}$	$2.15(17) \times 10^{-27}$	$1.78(77) \times 10^{-28}$	$1.75(56) \times 10^{-28}$
1	$3.4(1.3) \times 10^{-22}$	$2.07(17) \times 10^{-25}$	$1.88(81) \times 10^{-26}$	$1.86(59) \times 10^{-26}$
1.5	$6.6(2.5) \times 10^{-16}$	$2.03(16) \times 10^{-18}$	$2.4(1.0) \times 10^{-19}$	$2.52(81) \times 10^{-19}$
2	$5.7(2.2) \times 10^{-12}$	$4.15(33) \times 10^{-14}$	$6.5(2.8) \times 10^{-15}$	$7.1(2.3) \times 10^{-15}$
2.5	$3.3(1.3) \times 10^{-9}$	$3.99(32) \times 10^{-11}$	$8.7(3.7) \times 10^{-12}$	$7.9(2.5) \times 10^{-12}$
3	$3.6(1.4) \times 10^{-7}$	$6.40(51) \times 10^{-9}$	$1.75(75) \times 10^{-9}$	$1.10(35) \times 10^{-9}$
3.5	$1.18(45) \times 10^{-5}$	$3.02(24) \times 10^{-7}$	$9.4(4.0) \times 10^{-8}$	$3.9(1.3) \times 10^{-8}$
4	$1.73(66) \times 10^{-4}$	$5.82(46) \times 10^{-6}$	$1.92(83) \times 10^{-6}$	$5.6(1.8) \times 10^{-7}$
5	$7.6(2.9) \times 10^{-3}$	$3.5(2.8) \times 10^{-4}$	$1.19(51) \times 10^{-4}$	$2.17(69) \times 10^{-5}$
6	$8.7(3.3) \times 10^{-2}$	$4.68(38) \times 10^{-3}$	$1.52(66) \times 10^{-3}$	$2.58(83) \times 10^{-4}$
7	$4.3(1.7) \times 10^{-1}$	$2.88(23) \times 10^{-2}$	$8.8(3.8) \times 10^{-3}$	$1.79(57) \times 10^{-3}$
8	$1.23(47) \times 10^{0}$	$1.19(10) \times 10^{-1}$	$3.5(1.5) \times 10^{-2}$	$8.7(2.8) \times 10^{-3}$
9	$2.46(95) \times 10^{0}$	$3.83(31) \times 10^{-1}$	$1.11(48) \times 10^{-1}$	$3.05(98) \times 10^{-2}$
10	$4.0(1.6) \times 10^{0}$	$9.60(77) \times 10^{-1}$	$2.8(1.2) \times 10^{-1}$	$8.0(2.6) \times 10^{-2}$
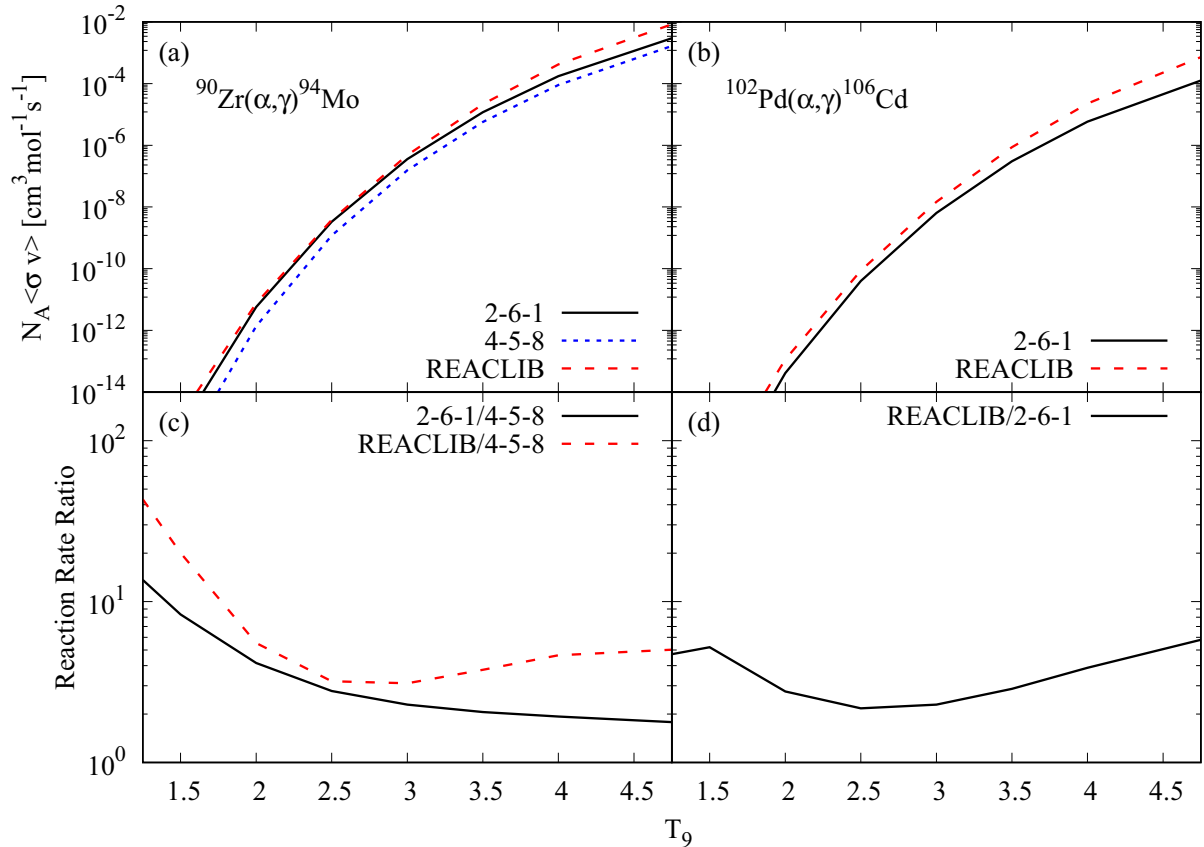
FIG. 4. (a) Reaction rates for ^{90}Zr$(\alpha, \gamma)^{94}$Mo. The blue (short dashed) line shows the TALYS combination that provided the best fit for the measured cross sections. The black (solid) line shows the reaction rate from the recommended TALYS combination. The red (dashed) line shows the rate given by the REACLIB database. (b) Reaction rates for ^{102}Pd$(\alpha, \gamma)^{106}$Cd. The black (solid) line shows the recommended TALYS combination, which is also the combination that provided the best fit for this reaction. The red (dashed) line shows the rate given by REACLIB. (c) The ratios of the recommended model combination to the best-fit model combination (black, solid) as well as the ratio of the REACLIB model to the best-fit model (red, dashed) for the ^{90}Zr$(\alpha, \gamma)^{94}$Mo reaction. (d) The ratio of the recommended model combination to the REACLIB model for the ^{102}Pd$(\alpha, \gamma)^{106}$Cd reaction. The numbers in the legends refer to the LD-αOMP-γSF models used in the TALYS calculations.

The γSF of all transitions except for the $E1$ transition are calculated using the Brink-Axel Lorentzian [27,28]. For the $E1$ γSF there are eight different options:

(1) the Kopecky-Uhl generalized Lorentzian [29],
(2) the Brink-Axel Lorentzian,
(3) the microscopic Hartree-Fock BCS tables [30],
(4) the microscopic Hartree-Fock-Bolgubyubov (HFB) tables [30],
(5) Goriely's hybrid tables [31],
(6) Goriely's temperature-dependent HFB [21],
(7) the temperature-dependent relativistic mean field [32], and
(8) the Gogny D1M HFB and quasiparticle random-phase approximation [33].

The default option for the $E1$ γSF is the Brink-Axel Lorentzian.

For the calculations in this work, microscopic models and macroscopic models were considered separately and mixtures of the two were not used when generating the model combinations. In all calculations, the knockout and stripping options

were turned off for neutrons and protons. In addition, the breakup option was turned off for neutrons, protons, and α particles. The semimicroscopic OMP of Jeukenne-Lejeune-Mahaux [34] for protons and neutrons was used for the calculations. Also, the option to scale the γSF to experimental values when known was disabled to allow for true comparison between models. For each reaction, TALYS calculations were run for each possible combination of LD, αOMP, and γSF model. To distinguish the combinations the notation LD-αOMP-γSF is used throughout the paper. For example 1-2-3 would refer to the combination of the constant temperature with Fermi gas LD model, the McFadden and Satchler αOMP, and the microscopic Hartree-Fock BCS tables for the γSF.

To determine the model combination that provided the best description of the data the χ^2 value for each model combination was calculated. The χ^2 was calculated using

$$\chi^2 = \Sigma \left(\frac{\sigma_{\text{exp}} - \sigma_{\text{th}}}{\delta\sigma_{\text{exp}}} \right)^2, \tag{3}$$

where σ_{exp} is the measured cross-section value, σ_{th} is the theoretical cross-section value of the model being tested,
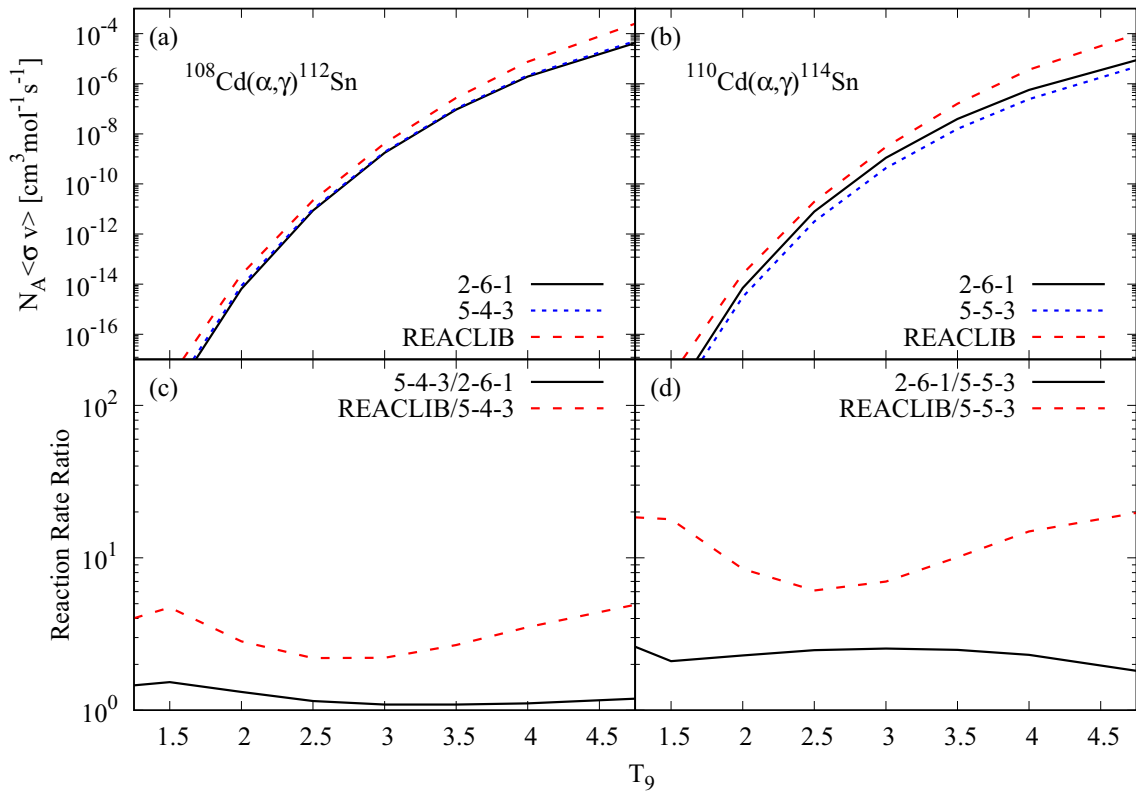
FIG. 5. (a) Reaction rates for ^{108}Cd$(\alpha, \gamma)^{112}$Sn. The blue (short dashed) line shows the TALYS combination that provided the best fit for the measured cross sections. The black (solid) line shows the reaction rate from the recommended TALYS combination. The red (long dashed) line shows the rate given by the REACLIB database. (b) Reaction rates for ^{110}Cd$(\alpha, \gamma)^{114}$Sn. The blue (short dashed) line shows the TALYS combination the provided the best fit for the reaction. The black (solid) line shows the reaction rate from the recommended TALYS combination. The red (long dashed) line shows the rate given by the REACLIB database. (c) The ratios of the recommended model combination to the best-fit model combination (black, solid) as well as the ratio of the REACLIB model to the best-fit model (red, dashed) for the ^{108}Cd$(\alpha, \gamma)^{112}$Sn reaction. (d) The ratios of the recommended model combination to the best-fit model combination (black, solid) as well as the ratio of the REACLIB model to the best-fit model (red, dashed) for the ^{110}Cd$(\alpha, \gamma)^{114}$Sn reaction. The numbers in the legends refer to the LD-αOMP-γSF models used in the TALYS calculations.

and $\delta\sigma_{\exp}$ is the uncertainty in the measured cross-section value.

The parameter combination that was found to best fit each reaction individually is plotted as a solid colored line in Fig. 3. For the ^{90}Zr$(\alpha, \gamma)^{94}$Mo cross-section data the χ^2 value for each combination was calculated with respect to the data in this work as well as the previous measurements from Quinn *et al.* [6]. From this, the parameter combination 4-5-8 was determined to provide the best description for the ^{90}Zr$(\alpha, \gamma)^{94}$Mo data. The best-fit model to the ^{102}Pd$(\alpha, \gamma)^{106}$Cd cross-section values given in this work is the combination 2-6-1. The best-fit model to the ^{108}Cd$(\alpha, \gamma)^{112}$Sn cross-section values given in this work is the combination 5-4-3. Due to the large discrepancy between the ^{108}Cd$(\alpha, \gamma)^{112}$Sn results given in this work and the previous measurements of this reaction, only the values obtained in this work were used to determine the best-fit model. For the ^{110}Cd$(\alpha, \gamma)^{114}$Sn values the best fit model was 5-5-3.

To determine one model that best described all four reactions, the χ^2 values for several thresholds were calculated. These can be seen in Table III. The thresholds were used as a measure of how much each model combination differed

from the measured values. For example, the 50% threshold was calculated by using Eq. (3) and setting $\sigma_{\text{th}} = 1.5\sigma_{\exp}$. So then a combination that has a χ^2 value less than the 50% threshold would be within a factor of 0.5–1.5 of the measured values, and a combination that has a χ^2 value within the 10% threshold would be within a factor of 0.9–1.1 of the measured values. From this, the model combination 2-6-1 was found to be able to describe all of the data within the 50% threshold, in addition to providing the best fit to the ^{102}Pd$(\alpha, \gamma)^{106}$Cd data. The combination 2-6-1 is the back-shifted Fermi gas LD model with the αOMP from Avrigeanu *et al.* [24] and the Brink-Axel Lorentzian γSF. From this, the combination 2-6-1 is recommended for predicting cross sections within this mass range.

Because the combination 2-6-1 is able to describe all four reactions within the 50% χ^2 threshold, this means that this combination is able to describe all of the measured cross-section values on average within a factor of 0.5–1.5.

V. DISCUSSION

For each measured reaction, the astrophysical reaction rate was calculated using the combination that best fit that
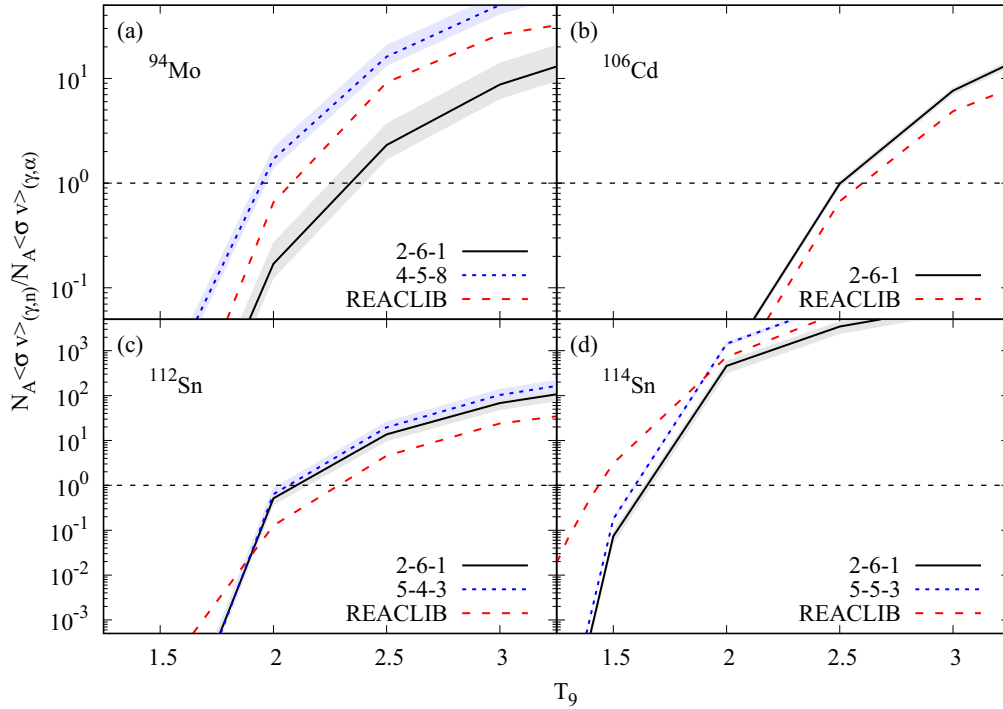
FIG. 6. Ratios of the (γ, n) reaction rates to the (γ, α) reaction rates for (a) ^{94}Mo, (b) ^{106}Cd, (c) ^{112}Sn, and (d) ^{114}Sn. The red (long dashed) line give the rates from the REACLIB database, the blue (short dashed) line gives the (γ, n) and (γ, α) rates calculated in TALYS using the model combination that best fits the individual reaction, and the black (solid) line is the (γ, n) and (γ, α) rates calculated in TALYS using the recommended reaction rates. The black dashed line indicates the point at which the (γ, α) rate becomes stronger than the (γ, n) rate for each model. The uncertainty bands correspond to the χ^2 percentage that the model combination achieved for the given reaction. The numbers in the legends refer to the LD-αOMP-γSF models used in the TALYS calculations.

reaction, as well as the recommended combination. The recommended reaction rate calculated using 2-6-1 as well as uncertainties based upon the threshold percentage that the model achieved for each reaction are given for the four reactions in Table IV. These reaction rates are plotted in the top panels of Figs. 4 and 5. The reaction rates given in the REACLIB database [35] using the NONSMOKER code are also plotted in the top panels of Figs. 4 and 5. In the bottom panels of Figs. 4 and 5, the ratios between the REACLIB rate and the best-fit rate as well as the ratios between the recommended rate and the best-fit rate are plotted. In all cases, the recommended rate can be seen to provide a much closer description of the best-fit rate than the REACLIB rate. In general, REACLIB is only able to describe measured cross sections within a factor of 2–20. In the case of the ^{90}Zr$(\alpha, \gamma)^{94}$Mo and ^{110}Cd$(\alpha, \gamma)^{114}$Sn reactions, the model combination 2-6-1 overpredicts the rate when compared to the best-fit combination. However, in the case of the ^{108}Cd$(\alpha, \gamma)^{112}$Sn reaction, the 2-6-1 model combination underpredicts the rate when compared to the best-fit combination. The recommended reaction rate is always within a factor of 10 from the best-fit rate, and in the case of ^{108}Cd$(\alpha, \gamma)^{112}$Sn it is within a factor of 2. The discrepancy stems from the integral of the cross section below the (α, n) channel threshold where no data are available.

Through the use of the principle of detailed balance, the rates for the (α, γ) forward reactions can be used to calculate the rates for the inverse (γ, α) reactions [36]. To determine if these are indeed branching points, the temperature where the

(γ, α) rate becomes stronger than the (γ, n) rate was investigated. The (γ, n) rates were calculated in TALYS using the same model combinations as for the (α, γ) and (γ, α) rates. This can be seen in Fig. 6. The uncertainty bands in Fig. 6 correspond to the percentages that the χ^2 values for each model achieved. In all cases the recommended reaction rates show that the (γ, α) rate begins to dominate over the (γ, n) rate within the temperature range of 1.5–3.5 T_9. In the case of ^{94}Mo, a strong dependence of the branching temperature on the model used can be seen. Regardless of the chosen model, ^{94}Mo is indeed a branching point. The results for ^{114}Sn show that with our best-fit model this isotope is indeed a branching point at low temperatures, while it is not a branching point when using the data from the REACLIB database. This means that at low temperatures the Cd isotopes that are more proton rich than ^{110}Cd will not be formed via a chain of (γ, n) reactions. This may alter the mass flow in the region during the end of the supernova shock wave. The full effects of this will be studied in our future work by using these rates in network calculations.

VI. CONCLUSIONS

Four different (α, γ) reactions have been measured and compared to different theoretical models. The cross sections were measured at the NSL using the γ-summing detector HECTOR. The reactions were measured using the γ-summing technique in an energy range of $E_{c.m.} = 7.5$–

11.5 MeV. The ^{90}Zr$(\alpha, \gamma)^{94}$Mo and ^{108}Cd$(\alpha, \gamma)^{112}$Sn reactions were both measured previously [6,10] and comparisons between this work and the previous work are given here. These measurements also extended the range of measured cross-section values down to lower energies for both reactions. The ^{102}Pd$(\alpha, \gamma)^{106}$Cd and the ^{110}Cd$(\alpha, \gamma)^{114}$Sn reactions were measured for the first time. All measured cross-section results fell below the predictions of the NONSMOKER code. The cross-section measurements were then compared to different combinations of LD, αOMP, and γSF models available in the TALYS 1.9 package.

It was determined that the combination of the back-shifted Fermi gas LD model with the αOMP from Avrigeanu *et al.* [24] and the Brink-Axel Lorentzian γSF reproduced all of the measured results within 50%. The ^{90}Zr, ^{102}Pd, and ^{108}Cd (α, γ) reactions were identified in a sensitivity study by

Rauscher [3] as being sensitive branching points for the reaction flows in γ-process reaction networks. The effect that the recommended model has on the branching temperature of each of the isotopes was explored and it was found that with this model all of the isotopes are branching points within the $T_9 = 1.5$–3.5 temperature range.

ACKNOWLEDGMENTS

[1] E. M. Burbidge, G. R. Burbidge, W. A. Fowler, and F. Hoyle, Rev. Mod. Phys. **29**, 547 (1957).

[2] S. E. Woosley and W. M. Howard, Astrophys. J. Suppl. Ser. **36**, 285 (1978).

[3] T. Rauscher, Phys. Rev. C **73**, 015804 (2006).

[4] Notre Dame Nuclear Science Laboratory, www.isnap.nd.edu (June 2019).

[5] M. Mayer, *Report IPP 9/113*, Max-Planck-Instiut für Plasmaphysik, Garching, Germany, 1997.

[6] S. J. Quinn *et al.*, Phys. Rev. C **92**, 045805 (2015).

[7] National Isotope Development Center, isotopes.gov (June 2019).

[8] C. S. Reingold *et al.*, Eur. Phys. J. A **55**, 77 (2019).

[9] A. Spyrou, H.-W. Becker, A. Lagoyannis, S. Harissopulos, and C. Rolfs, Phys. Rev. C **76**, 015802 (2007).

[10] P. Scholz, F. Heim, J. Mayer, C. Münker, L. Netterdon, F. Wombacher, and A. Zilges, Phys. Lett. B **761**, 247 (2016).

[11] P. Scholz (private communication).

[12] T. Rauscher and F.-K. Thielemann, At. Data Nucl. Data Tables **79**, 47 (2001).

[13] P. Demetriou, C. Grama, and S. Goriely, Nucl. Phys. A **707**, 253 (2002).

[14] A. J. Koning, S. Hilaire, and M. C. Duijvestijn, "TALYS-1.0", in *Proceedings of the International Conference on Nuclear Data for Science and Technology*, April 22-27, 2007, Nice, France, edited by O. Bersillon, F. Gunsing, E. Bauge, R. Jacqmin, and S. Leray (EDP Sciences, 2008), pp. 211–214.

[15] A. Gilbert and A. G. W. Cameron, Can. J. Phys. **43**, 1446 (1965).

[16] W. Dilg, W. Schantl, H. Vonach, and M. Uhl, Nucl. Phys. A **217**, 269 (1973).

[17] A. V. Ignatyuk, K. K. Istekov, and G. N. Smirenkin, Sov. J. Nucl. Phys. **29**, 450 (1979).

[18] A. V. Ignatyuk, J. L. Weil, S. Raman, and S. Kahane, Phys. Rev. C **47**, 1504 (1993).

[19] S. Goriely, F. Tondeur, and J. Pearson, At. Data Nucl. Data Tables **77**, 311 (2001).

[20] S. Goriely, S. Hilaire, and A. J. Koning, Phys. Rev. C **78**, 064307 (2008).

[21] S. Hilaire, M. Girod, S. Goriely, and A. J. Koning, Phys. Rev. C **86**, 064317 (2012).

[22] A. Koning and J. Delaroche, Nucl. Phys. A **713**, 231 (2003).

[23] L. McFadden and G. R. Satchler, Nucl. Phys. **84**, 177 (1966).

[24] V. Avrigeanu, M. Avrigeanu, and C. Mănăilescu, Phys. Rev. C **90**, 044612 (2014).

[25] M. Nolte, H. Machner, and J. Bojowald, Phys. Rev. C **36**, 1312 (1987).

[26] V. Avrigeanu, P. E. Hodgson, and M. Avrigeanu, Phys. Rev. C **49**, 2136 (1994).

[27] P. Axel, Phys. Rev. **126**, 671 (1962).

[28] D. M. Brink, Nucl. Phys. **4**, 215 (1957).

[29] J. Kopecky and M. Uhl, Phys. Rev. C **41**, 1941 (1990).

[30] R. Capote *et al.*, Nucl. Data Sheets **110**, 3107 (2009).

[31] S. Goriely, Phys. Lett. B **436**, 10 (1998).

[32] D. Pena Arteaga and P. Ring, Phys. Rev. C **77**, 034317 (2008).

[33] M. Martini, S. Hilaire, S. Goriely, A. J. Koning, and S. Péru, Nucl. Data Sheets **118**, 273 (2014).

[34] J.-P. Jeukenne, A. Lejeune, and C. Mahaux, Phys. Rev. C **15**, 10 (1977).

[35] REACLIB Database, reaclib.jinaweb.org (June 2019).

[36] T. Rauscher and F.-K. Thielemann, At. Data Nucl. Data Tables **75**, 1 (2000).